Journal of The Electrochemical Society, 2023 **170** 060504
1945-7111/2023/170(6)/060504/7/$40.00

In Situ Growth of NiCoSe Nanoparticles/Holey Carbon Nanosheet on Carbon Cloth as an Efficient Sulfur Host for Flexible Li–S Batteries

He Wang,[1] Han Su,[1] Hongling Guo,[1] Mingzhi Yang,[1] Weiliang Liu,[1] Jinshui Yao,[1] Manman Ren,[1,z] and Yuanhao Wang[2,z]

[1]*School of Materials Science and Engineering, Qilu University of Technology (ShandongAcademy of Sciences), Jinan 250353, People's Republic of China*
[2]*Hoffmann Institute of Advanced Materials, Shenzhen Polytechnic, 7098 Liuxian Boulevard, Nanshan District, Shenzhen 518055, People's Republic of China*

Recently, commercial wearable electronic devices have gradually attracted research interest in flexible batteries. The electrode is the crucial component of a flexible lithium-sulfur battery, which restricts the development of flexible lithium-sulfur batteries (LSBs). Here, NiCoSe/holey carbon nanosheet in situ grown on carbon cloth (NiCoSe/CNS/CC) was successfully synthesized and used as an efficient sulfur host for the flexible sulfur cathode. Its special structure also provides optimal conditions for the loading of sulfur and promotes efficient transport of both electrons and Li-ions. Numerous polar NiCoSe nanoparticles are attached to the surface of carbon fibers, which can effectively anchor lithium polysulfides (LiPSs) by chemisorption and accelerate their conversion. Benefiting from this special architecture and the polar NiCoSe nanoparticles, the NiCoSe/CNS/CC/S demonstrates excellent electrochemical performance. At 1C, the NiCoSe/CNS/CC/S electrode delivers a discharge capacity of 454 mA h g^{-1} after 600 cycles. Furthermore, even at 2C, after 600 cycles, it still maintains a capacity of 426 mA h g^{-1}, with a capacity decay of 0.079% per cycle. The NiCoSe/CNS/CC/S electrode enriches the flexible sulfur cathodes with its excellent electrochemical and mechanical properties while providing a new path for the research of flexible LSBs.
 [DOI: 10.1149/1945-7111/acd816]

Manuscript submitted February 15, 2023; revised manuscript received May 10, 2023. Published June 1, 2023.

Supplementary material for this article is available online

In recent years, the growing popularity of commercial wearable electronic devices has led to research interest in flexible batteries.[1] Among the various alternatives for the new energy storage equipment, lithium-sulfur batteries (LSBs) have gained attention due to their desirable theoretical capacity/energy density (1675 mA h g^{-1}/2600 Wh kg^{-1}) and low cost.[2,3] The application of flexible LSBs holds great promise for improving the high energy density of flexible devices. However, the development of flexible electrodes remains a major obstacle to the commercialization of flexible batteries. Accelerating the progress toward commercialization for flexible batteries, it is crucial to study flexible electrode materials that offer high capacity, low cost, and excellent mechanical properties.[4,5]

Flexible electrodes need to maintain stable electrochemical performance even when repeatedly bent, folded, and stretched. However, conventional cathode materials used in LSBs are typically inflexible.[6] CC is regarded as an optimal material for flexible electrodes due to its exceptional conductivity and mechanical properties.[7,8] Carbon-based flexible electrodes, such as carbon cloth (CC),[9,10] carbon nanotubes,[11,12] and graphene,[13] have been extensively studied. Nowadays, flexible CC has been applied in LSBs.[14,15] For example, Ran Elazari et al. prepared a binder-free carbon-sulfur cathode by melting sulfur and microporous activated carbon fiber cloth, and the CC/S cathode could maintain a discharge capacity above 800 mA h g^{-1} after 80 cycles.[16]

While CC has been a host material to enhance the electrochemical properties of sulfur electrodes, the weak physical adsorption between non-polar CC and polar lithium polysulfide (LiPSs) cannot effectively inhibit the shuttle of LiPSs.[17] Recently, it is reported that polar metal compounds (metal selenides, metal sulfides, metal phosphides, etc.) can anchor LiPSs through chemisorption and effectively inhibit the "shuttle effect."[18–22] Transition metal selenide sulfur hosts have garnered significant attention due to the similar physical and chemical properties between sulfur and selenium,[23–26] and the bimetallic metal selenides have been extensively investigated since they can offer more adsorption active sites than single metal selenides.[27,28] As a successful example, Zhang et al. synthesized a sea urchin-like $NiCo_2Se_4$ (u-NCSe) and loaded it with sulfur, which exhibited high capacities (1330 and 626 mA h g^{-1} at 0.1C and 5C rates).[29] Therefore, the construction of CC and bimetallic transition metal selenides composites may be an ideal way to prepare flexible LSBs sulfur cathodes.

Herein, a composite of NiCoSe nanoparticles/holey carbon nanosheet in situ grown on carbon cloth (NiCoSe/CNS/CC) was prepared via a solvothermal method. The unique structure of the material provides optimal conditions for the loading of sulfur and promotes efficient transport of both electrons and Li-ions. SEM and TEM images demonstrate that numerous polar NiCoSe nanoparticles are attached to the surface of carbon fibers. NiCoSe nanoparticles can effectively adsorb LiPSs by chemical adsorption and accelerate their conversion.[30] Due to the peculiar structure and the presence of polarity NiCoSe nanoparticles, the NiCoSe/CNS/CC/S electrodes exhibit excellent electrochemical properties. Even when tested at 2C, after 600 cycles, the NiCoSe/CNS/CC/S electrode can maintain a reversible capacity of 426 mA h g^{-1}, with the capacity decay as low as 0.079% per cycle. The NiCoSe/CNS/CC/S electrode enriches the flexible LSBs cathode materials with its excellent electrochemical and mechanical properties, meanwhile, it also provides a new path for the research of flexible LSBs.

Experimental

Preparation of NiCoSe/CNS/CC.—Firstly, a piece of carbon cloth (CC) was treated with acetone, ethanol, and deionized water for 20 min, respectively. Next, the CC was dried at 80 °C and then calcined in Ar at 900 °C for 2 h.

The NiCoSe/CNS/CC was prepared through the following steps: First, 5 mM of $Co(NO_3)_2{\cdot}6H_2O$ and 5 mM of $Ni(NO_3)_2{\cdot}6H_2O$ were added to 20 ml of methanol solution and stirred to prepare solution A. Secondly, 20 mM of 2-methylimidazole was added to 20 ml of methanol solution and stirred to prepare solution B. Solutions A and B were mixed and stirred for 30 min. And then, the pretreated CC and the mixture were transferred to a reaction kettle and kept at 120 °C for 14 h in a solvothermal process. Afterward, the product was washed

[z]E-mail: renmanman@qlu.edu.cn; wangyuanhao@szpt.edu.cn

with ethanol, and dried at 80 °C. Finally, the dried product and selenium powder were reacted at 600 °C for 2 h to obtain the NiCoSe/CNS/CC.

Preparation of NiCoSe/CNS/CC/S and CC/S electrodes.— Preparation of NiCoSe/CNS/CC/S: Firstly, NiCoSe/CNS/CC was cut into a rectangle of 3 × 1.5 cm. Next, 0.35 g of S powder was added to 10 ml of CS_2 and stirred to form a solution. Then, the pre-cut NiCoSe/CNS/CC (3 × 1.5 cm) was soaked in the prepared solution for 5 min, and the NiCoSe/CNS/CC/S was obtained by removing the CS_2 solution. CC/S was synthesized using the same procedure.

Li_2S_6 adsorption test.—Preparation of Li_2S_6 solution: Li_2S and S with a molar ratio of 1:5 were dissolved in a solution of DME/DOL (v/v = 1:1), followed by continuous stirring at 60 °C for 24 h. Next, CC and NiCoSe/CNS/CC with the same size were added to glass vials containing 2 ml of Li_2S_6 solution, and then the solution was sealed and placed for 12 h.

Material characterization.—The morphologies of the samples were characterized by SEM (ZEISS G500) and TEM (HRTEM, Tecnai G2F30 S-Twin) (the acceleration voltages of the SEM and TEM tests are 5∼15 and 200 kV, respectively), and the element distribution of the NiCoSe/CNS/CC was determined by EDS test. Shimadzu XRD-6100AS X-ray diffractometer (XRD, Cu Kα, λ = 0.154 nm) was used to analyze the crystal structure of the samples. Raman was measured using a LabRam HR Raman spectrometer (laser wavelength is 532.03 nm). Li_2S_6 adsorption experiments were carried out using a UV spectrophotometer (TU-1901). Nitrogen adsorption isotherms were determined by a Micromeritcs Gemini V2380 analyzer at 77 K (BET mathematical model was used to calculate the specific surface area of the samples). X-ray photoelectron spectroscopy (XPS) analysis was performed using an ESCALAB 250 spectrometer (X-ray emission source: Mg Kα, step size: 0.05 eV).

Electrochemical test.—The as-prepared NiCoSe/CNS/CC/S and CC/S were used directly as cathodes for LSBs. Lithium sheet and PP were used as the anode and separator, respectively. The electrolyte was 1.0 M LiTFSI dissolved in DME/DOL solution (v/v = 1:1), which contained 1.0% $LiNO_3$. The low sulfur loading was 1.2 mg cm^{-2}, and the high sulfur loading was 3.2 mg cm^{-2}. The cycle and rate-performances were performed on the Neware battery test system at different C rates (1C = 1675 mA g^{-1}); the current densities of 0.1, 0.2, 0.5, 1, 2, and 3C in this work were 167.5, 335, 837.5, 1675, 3350, and 5025 mA g^{-1}, respectively. The test potential range was 1.7∼2.8 V. Cyclic Voltammetry (CV) and electrochemical impedance spectroscopy (EIS) tests were carried out on CHI760E Electrochemical Workstation.

Results and Discussion

NiCoSe/CNS/CC was synthesized through a simple solvothermal reaction, and the preparation process is shown in Fig. 1. Firstly, CC was immersed in a methanol solution that contained cobalt nitrate hexahydrate, nickel nitrate hexahydrate, and 2-methylimidazole; next, the mixture was transferred to an autoclave and reacted at 120 °C for 14 h. During the solvothermal process, the cobalt and nickel precursors uniformly grew on the carbon fibers to form a Ni–Co–CC intermediate. Finally, the Ni–Co–CC intermediate reacted with selenium powder at 600 °C for 2 h to obtain the NiCoSe/CNS/CC.

The morphologies of CC and NiCoSe/CNS/CC were characterized by SEM, which revealed that the CC is woven from carbon fibers with diameters of about 10 μm (Figs. 2a and 2b), and the flat surface of carbon fibers is conducive to the loading of heterogeneous materials. The low-resolution SEM image of NiCoSe/CNS/CC (Fig. 2c) demonstrates that the carbon fibers are covered with holey nanosheets. The high-resolution SEM image of NiCoSe/CNS/CC illustrates that numerous nanoparticles are evenly attached to the surface of the holey nanosheets (Fig. 2d).

TEM test was employed to explore the surface microstructure of NiCoSe/CNS/CC. As shown in Figs. 2e–2g, numerous nanoparticles with a size of ∼90 nm are homogeneously attached to the thin and wrinkled nanosheet. In addition, the special structure involves the reaction between $Ni(NO_3)_2{\cdot}6H_2O$/$Co(NO_3)_2{\cdot}6H_2O$ and 2-methylimidazole, during which organic ligands are formed. These organic ligands are used as growth templates for the in situ growth of holey nanosheets decorated with Ni–Co. Therefore, the layered three-dimensional nanoparticle/holey carbon nanosheet structure is formed during the solvothermal process.[31,32] The lattice spacing of 0.26 nm in HRTEM correlates with the (210) crystal plane of $NiSe_2$ and $CoSe_2$ (Fig. 2h). Meanwhile, EDS element mappings exhibit that C is distributed throughout the whole structure (Fig. 2j). Co, Ni, and Se elements are evenly distributed in nanoparticles (Figs. 2k–2m). Combined with the HRTEM result, it is inferred that the nanoparticles are composed of $NiSe_2$ and $CoSe_2$.

NiCoSe/CNS/CC was studied by XRD to explore the chemical composition and crystal form. As shown in Fig. 3a, all diffraction peaks are consistent with cubic $NiSe_2$ (JCPDS No. 65-5016) and cubic $CoSe_2$ (JCPDS No. 65-3327),[33] indicating the high purity of the composite. No obvious carbon peak is detected due to the amorphous nature of carbon. Additionally, the strong peak illustrates the high crystallinity of the composite. Raman spectroscopy was performed to study the carbon structure in NiCoSe/CNS/CC and CC. As shown in Fig. 3b, two broad peaks at 1337 and 1574 cm^{-1}, associated with the D and G bands of carbon, are observed in the Raman spectra. In general, the intensity ratio of D-band to G-band (I_D/I_G) can reflect the degree of disorder in carbon materials. NiCoSe/CNS/CC (1.133) exhibits a higher I_D/I_G value than that of CC (1.120), indicating a higher degree of disorders and defects in the NiCoSe/CNS/CC structure.[34] The N_2 adsorption/desorption isotherms presented in Fig. 3c belong to the H3 hysteresis type IV isotherm, illustrating the presence of mesoporous in NiCoSe/CNS/CC structure. Furthermore, the pore size distribution (inset in Fig. 3c) indicates that the pore size is predominantly 5 nm. The mesoporous structure facilitates the uniform dispersion of S and can promote the transport of Li^+ and electron.[35,36]

The chemical composition and valence state of NiCoSe/CNS/CC were investigated using the XPS test. Figure S1 presents the C 1 s XPS spectrum in NiCoSe/CNS/CC, where the four fitted peaks at 294.8, 286.1, 284.7, and 283.9 eV correspond to the O–C=O, C–O, C=C, and C–C bonds, respectively. Among them, the C–C and C=C bonds are derived from carbon fibers, while the presence of O–C=O and C–O bonds is due to contact with air during the preparation process.[37] The Ni 2p spectrum shows peaks attributed to Ni $2p_{1/2}$ and Ni $2p_{3/2}$ at 872.1 and 854.7 eV, respectively, confirming that the valence state of Ni in NiCoSe/CNS/CC is +2 (Fig. 3d). In addition, the other two peaks located at 878.9 and 860.4 eV are characteristic satellite peaks of Ni $2p_{1/2}$ and Ni $2p_{3/2}$, respectively.[38,39] The two peaks at 778.0 and 780.4 eV in Co 2p spectrum are correlated with Co $2p_{3/2}$, and the peaks at 792.9 and 796.4 eV are corresponding to Co $2p_{1/2}$, indicating that Co exists in the form of Co^{2+} in NiCoSe/CNS/CC (Fig. 3e). Additionally, the characteristic satellite peaks of Co $2p_{1/2}$ and Co $2p_{3/2}$ are detected at 802.1 and 784.7 eV, respectively.[28,35,40] The Se $3d_{3/2}$ and Se $3d_{5/2}$ are associated with broad peaks located at 54.7 and 53.8 eV, respectively. Meanwhile, the peak at 58.2 eV is attributed to the Se–O–Se bond generated due to surface oxidation during the preparation process (Fig. 3f).[27,37,41]

The electrochemical performance of the NiCoSe/CNS/CC/S and CC/S electrodes was investigated by using simulated batteries. Figure 4a demonstrates the CV curves of the two electrodes at 0.1 mV s^{-1}. For the NiCoSe/CNS/CC/S electrode, the two reduction peaks at 2.29 and 2.05 V are associated with the reduction process of S_8 to LiPSs and Li_2S, while the oxidation peak at 2.40 V corresponds to the oxidation process of Li_2S to LiPSs and S_8.[42] Additionally, compared with the CC/S electrode (368 mV), the potential

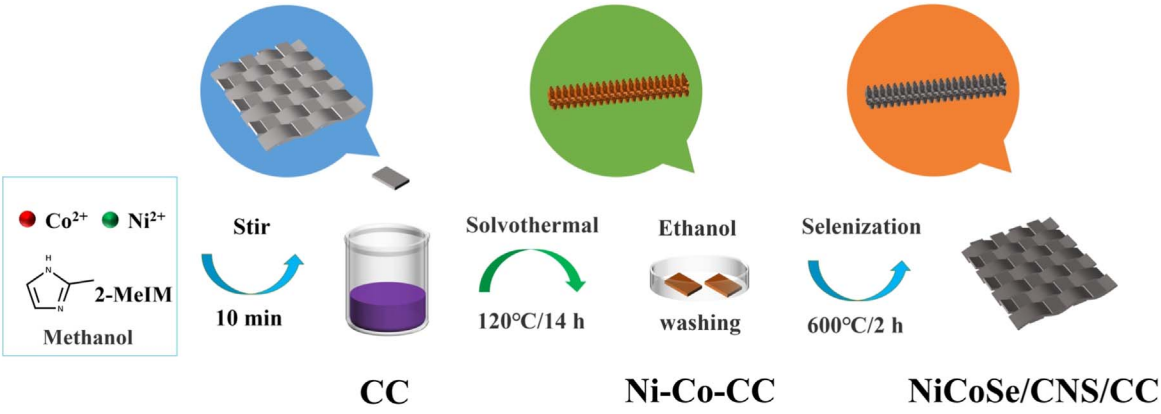

Figure 1. Synthetic illustration for the preparation of NiCoSe/CNS/CC.

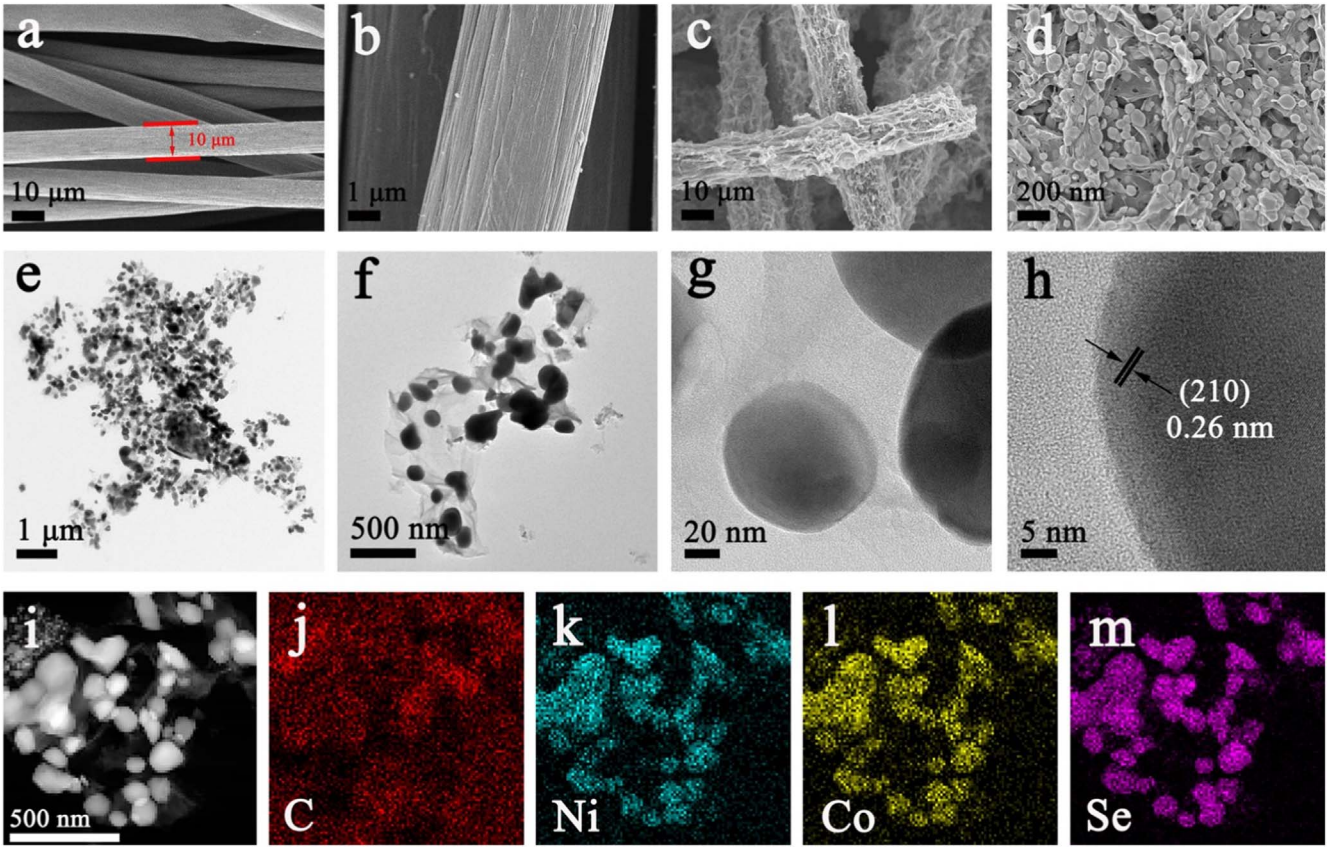

Figure 2. SEM images of (a), (b) CC and (c), (d) NiCoSe/CNS/CC. TEM and HRTEM images (e)–(h), and EDS elemental mappings (i)–(m) of the NiCoSe/CNS/CC.

difference between the reduction peak and the oxidation peak in the NiCoSe/CNS/CC/S electrode (354 mV) is smaller, suggesting that there are better dynamic properties in NiCoSe/CNS/CC/S electrode (Fig. 4a).[43] Moreover, Figs. S2 and S3 illustrate the better consistency of the CV curves for the NiCoSe/CNS/CC/S electrode, illustrating its better reversibility.

The discharge process of the sulfur cathode contains multi-step reactions, and the discharge capacity mainly comes from two reduction reactions at high potential (~2.3 V) and low potential (~2.1 V). The high potential reduction reaction is ascribed to the solid-liquid conversion of S_8 to LiPSs, while the low potential reduction reaction is attributed to the liquid-solid conversion of LiPSs to Li_2S.[44] Therefore, the low potential reduction reaction is affected by the long-chain LiPSs generated from the reduction reaction at a high potential. Compared with the NiCoSe/CNS/CC/S electrode (Fig. S2), the CC/S electrode has a significant difference in current intensities between the two cathodic peaks (Fig. S3). This phenomenon is attributed to the poor adsorption performance of CC toward long-chain LiPSs, which could not effectively limit the dissolution of LiPSs. Meanwhile, the weak adsorption performance of CC toward LiPSs affects the low potential reduction reaction, thus the capacity of the CC/S electrode would be lower in this process. On the contrary, for the NiCoSe/CNS/CC/S electrode, the current intensity of the reduction peak is much higher at low potential, confirming that the NiCoSe/CNS/CC has better adsorption and catalytic performance for LiPSs.[45] This result is also consistent with the CV profiles at different scan rates shown in Figs. 4b and 4c.

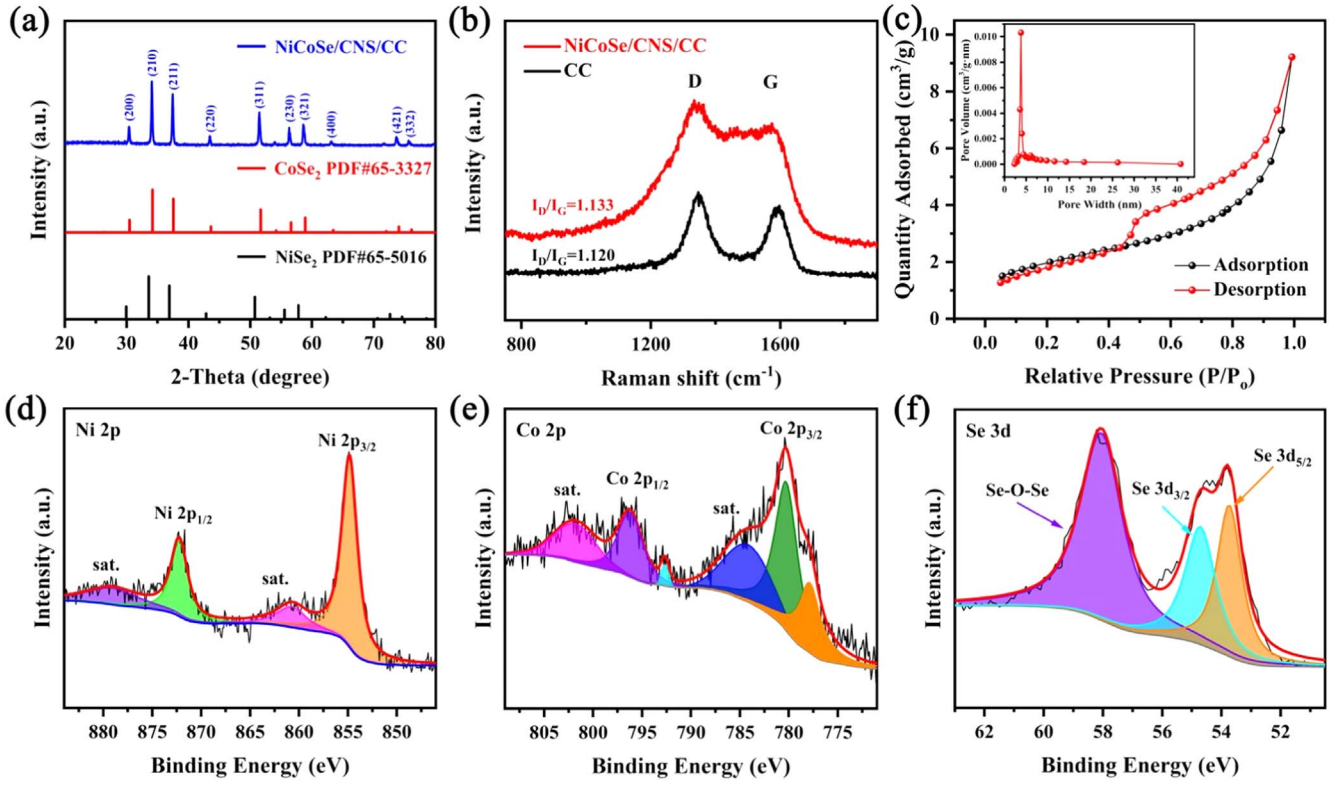

Figure 3. XRD patterns (a), Raman spectroscopy (b), and N_2 adsorption-desorption isotherms and pore size distribution (inset) (c) of the NiCoSe/CNS/CC. Ni 2p (d), Co 2p (e), and Se 3d (f) XPS spectra of the NiCoSe/CNS/CC.

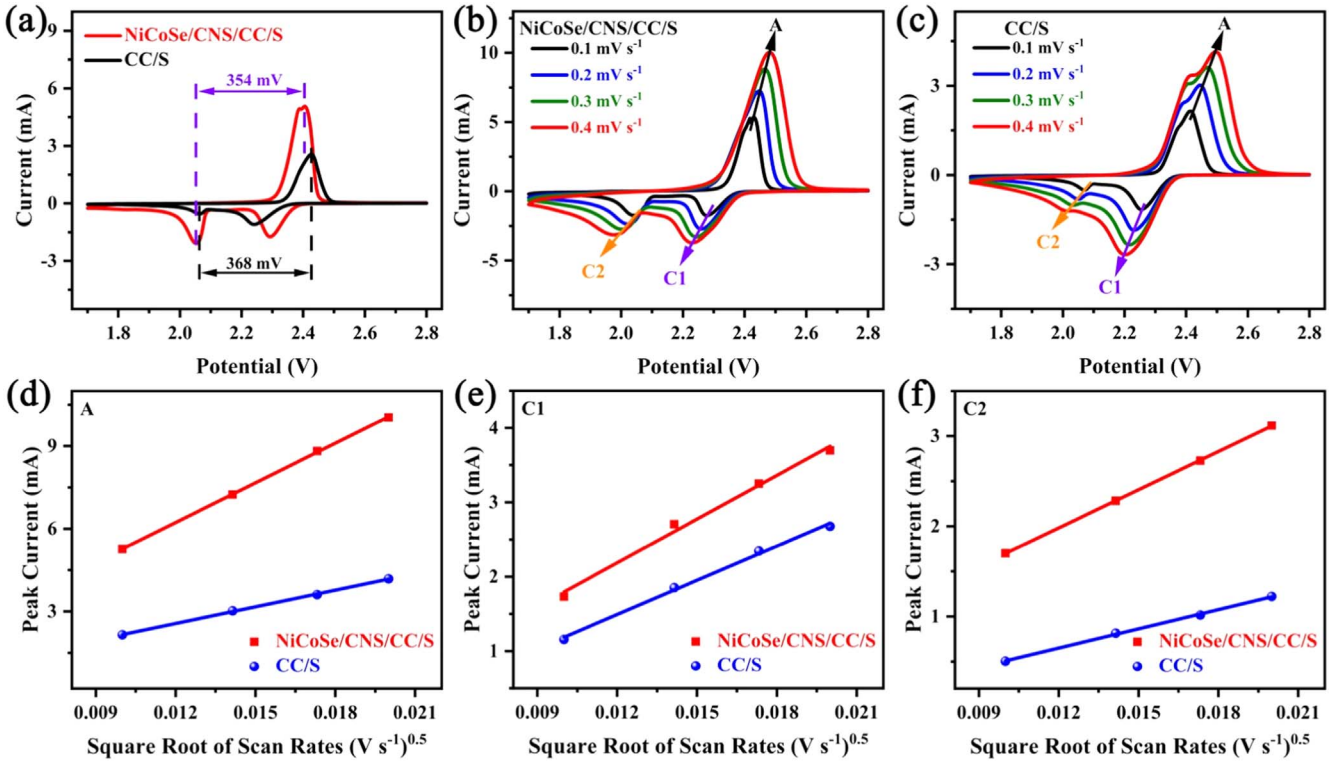

Figure 4. (a) CV curves of the two electrodes at 0.1 mV s^{-1}. CV curves of the NiCoSe/CNS/CC/S (b) and CC/S (c) electrodes at different scan rates. (d)–(f) The peak current values of peaks A, C1, and C2 vs the square root of scan rates of the NiCoSe/CNS/CC/S and CC/S electrodes.

It is a critical factor that the diffusion rate of Li-ion (D_{Li+}) could affect the redox kinetics of LiPSs. To investigate D_{Li+}, a CV test was conducted using the Randles-Sevcik equation: $I_p = (2.69 \times 10^5)$ $n^{3/2}AD^{1/2}C\nu^{1/2}$.[46–48] Where, I_p, n, A, D, C, and ν represent the peak current, the number of reaction electrons, the electrode area, the diffusion coefficient of Li-ion, the C_{Li+} in the electrolyte, and the

scan rate, respectively. According to the equation, the I_p is linearly related to the $\nu^{1/2}$. To this end, we tested the CV of the NiCoSe/CNS/CC/S and CC/S electrodes at different scan rates (Figs. 4b and 4c) with the same active sulfur. Based on the CV results, D_{Li+} is calculated and illustrated in Table SI. The D_{Li+} is faster in NiCoSe/CNS/CC/S electrodes.[47]

To explore the tolerance of NiCoSe/CNS/CC/S electrode to current changes, rate performances were investigated (Fig. 5a). At 0.1C, the NiCoSe/CNS/CC/S electrode can achieve a high discharge capacity of 1203 mA h g^{-1}. When the C rates are increased to 0.2, 0.5, 1, 2, and 3C, the specific capacities of NiCoSe/CNS/CC/S electrodes are 692, 588, 525, 451, and 391 mA h g^{-1}, respectively. However, the specific capacities of the CC/S electrode are much lower than that of the NiCoSe/CNS/CC/S electrode (350, 306, 237, 202, 172, 154 mA h g^{-1}). As the C rate returns to 0.1C, the specific capacity of the NiCoSe/CNS/CC/S electrode can be restored to 611 mA h g^{-1}. Additionally, there are reaction plateaus can be observed at each C rate from the charge-discharge profiles of NiCoSe/CNS/CC/S electrode under different C rates (Fig. S4), indicating that the NiCoSe/CNS/CC/S electrode possesses satisfactory reaction kinetics and desirable resistance to current variation.[49]

The long-cycling performances of the NiCoSe/CNS/CC/S and CC/S electrodes are shown in Fig. 5b. The initial discharge capacity of the NiCoSe/CNS/CC/S electrode has an initial discharge capacity of 1049 mA h g^{-1}, which can still be maintained at 454 mA h g^{-1} after 600 cycles, while the CC/S electrode illustrates a very low capacity (only 159 mA h g^{-1}). Furthermore, at 2C, the NiCoSe/CNS/CC/S electrode presents a discharge capacity of 426 mA h g^{-1} after 600 cycles with the capacity decay as low as 0.079% per cycle. At 0.5C, the NiCoSe/CNS/CC/S electrode can deliver a reversible capacity of 511 mA h g^{-1} after 400 cycles with an average decay rate of only 0.036% per cycle (Fig. S5), whereas the capacity of the CC/S electrode (194 mA h g^{-1}) is not satisfactory. Meanwhile, the cycling stability of the NiCoSe/CNS/CC/S electrode with a high sulfur loading has also been studied (Fig. 5c), and after 200 cycles, a reversible capacity of 399 mA h g^{-1} can still be maintained at 0.2C.

When doped with NiCoSe, the electrochemical performance of the CC/S electrode was improved, and the synergistic adsorption and catalysis of $NiSe_2$ and $CoSe_2$ promoted the conversion of LiPSs to Li_2S, which effectively inhibited the shuttle of LiPSs in the NiCoSe/CNS/CC/S electrode.[25,27,50] Furthermore, we also compared the electrochemical performance of reported CC-based sulfur electrodes with this work (Table SII), it is obvious that the NiCoSe/CNS/CC/S electrode exhibits better cycling stability.

Figure 6a shows the initial galvanostatic charge/discharge profiles of the NiCoSe/CNS/CC/S and CC/S electrodes at 1C. Both electrodes exhibit multiple plateaus, which are related to the multi-step transformations of sulfur in the electrochemical process. The charging and discharging plateaus correspond to the redox peaks of the CV curves. The plateaus of the NiCoSe/CNS/CC/S electrode

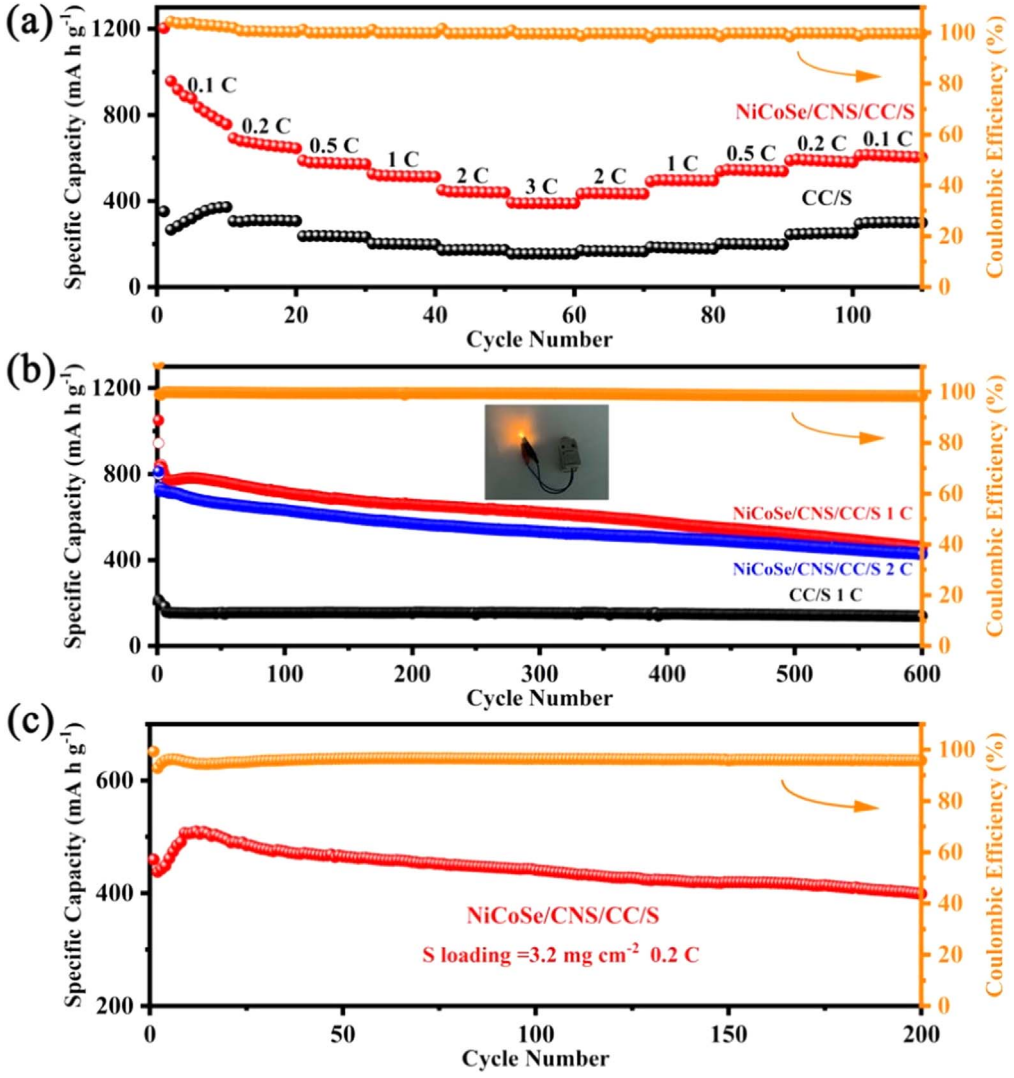

Figure 5. (a) Rate-performances and (b) Long-cycling performances of the NiCoSe/CNS/CC/S and CC/S electrodes. (c) Cycling stability of the NiCoSe/CNS/CC/S electrode with S loading of 3.2 mg cm^{-2} at 0.2C.

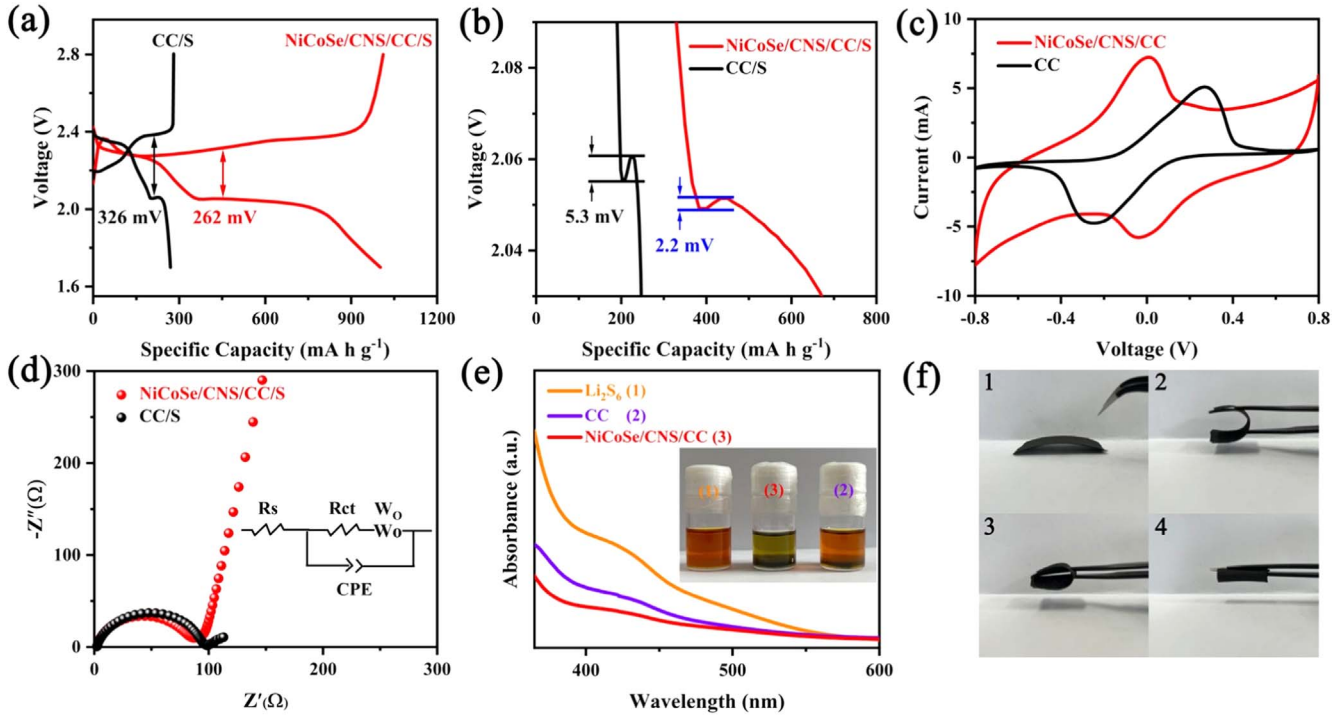

Figure 6. Galvanostatic discharge-charge profiles (a) and voltage dip at the nucleation site of Li_2S (b) in the first discharge process of the NiCoSe/CNS/CC/S and CC/S electrodes. (c) CV curves of symmetric batteries. (d) EIS Nyquist plots of the NiCoSe/CNS/CC/S and CC/S electrodes and the equivalent circuit (inset). (e) UV absorption spectra and Li_2S_6 adsorption test (inset) of the NiCoSe/CNS/CC and CC hosts. (f) Digital photos of the flexible NiCoSe/CNS/CC/S electrode.

are longer than that of the CC/S electrode, indicating that the NiCoSe/CNS/CC/S electrode has a higher capacity.[51] In addition, the NiCoSe/CNS/CC/S electrode demonstrates a smaller polarization voltage ($\Delta E = 262$ mV) than that of the CC/S electrode ($\Delta E =$ 326 mV), suggesting the better electrochemical reversibility of NiCoSe/CNS/CC/S electrode,[52] which is consistent with the CV test. Note that the voltage dip of the Li_2S nucleation site can reflect the nucleation dynamics of the sulfur cathode. The voltage dip of the CC/S electrode (5.3 mV) shown in Fig. 6b is higher than that of the NiCoSe/CNS/CC/S electrode (2.2 mV), indicating that NiCoSe can accelerate the nucleation and deposition of Li_2S, to accelerate the conversion of LiPSs and improve the utilization of sulfur.[47,53]

The contribution of two hosts to the sulfur redox kinetics was investigated using Li_2S_6 symmetric cells. The current response on the CV curve can evaluate the redox ability of Li_2S_6. As shown in Fig. 6c, the NiCoSe/CNS/CC exhibits a higher current response than that of the CC, indicating that the introduction of NiCoSe into CC can accelerate the conversion of Li_2S_6.[20,54] Figure 6d demonstrates the EIS Nyquist plots of these two electrodes. The EIS Nyquist plots exhibit a semicircle and an oblique line in the high-frequency and low-frequency regions, respectively, related to the charge transfer resistance (Rct) and Li^+ diffusion, respectively. The Rct of the NiCoSe/CNS/CC/S electrode is 84 Ω, which is lower than that of the CC/S electrode (96 Ω), illustrating that the presence of NiCoSe can further improve the electronic conductivity of the sulfur cathode.[10,45]

The adsorption capacities of two hosts toward LiPSs were investigated by Li_2S_6 adsorption and UV tests (Fig. 6e). It is observed that the color of the Li_2S_6 solution become lighter after adding NiCoSe/CNS/CC host for 12 h, while the color of Li_2S_6 solution with CC addition hardly changed (inset of Fig. 6e). Through analyzing the UV absorption spectra of NiCoSe/CNS/CC-Li_2S_6 and CC-Li_2S_6, it is obvious that the characteristic peak of the Li_2S_6 solution with NiCoSe/CNS/CC addition is significantly lower than that of the Li_2S_6 solution with CC addition in the region of 400∼500 nm, indicating the stronger adsorption capacity of NiCoSe/CNS/CC toward LiPSs.[55–57] The Li_2S_6 adsorption experiments confirmed the effective limitation of the "shuttle effect" in the presence of NiCoSe/CNS/CC. Figure 6f displays the digital photos of the NiCoSe/CNS/CC/S electrode. The electrode is not damaged after bending, folding, and curling tests, indicating its excellent mechanical and flexible properties. Therefore, the electrode can be used in flexible electronic devices.

Conclusions

In summary, the successful preparation of NiCoSe/CNS/CC composite as a host for flexible high-efficiency LSBs has been achieved. The unique structure of the holey nanosheet promotes uniform distribution of sulfur, allowing for efficient transport of Li^+ and electrons. Additionally, the carbon fiber surface is uniformly covered with polar NiCoSe nanoparticles, which could provide ample active sites for the chemisorption of LiPSs. Benefitting from the synergistic chemisorption and catalysis of the $NiSe_2$ and $CoSe_2$, the shuttle of LiPSs can be effectively inhibited. The NiCoSe/CNS/CC/S electrode exhibits excellent electrochemical performance; it could maintain a discharge capacity of 426 mA h g^{-1} at 2C after 600 cycles with a capacity decay rate of 0.079% per cycle. Additionally, the bending, folding, and crimping tests testified that the NiCoSe/CNS/CC/S electrode has superior mechanical and flexible properties. Owing to the excellent electrochemical and mechanical properties of NiCoSe/CNS/CC/S electrodes, this work will provide a new way of studying flexible LSBs.

Acknowledgments

This work was financially supported by the Natural Science Foundation of Shandong Province (Grant No. ZR2022ME062 and ZR2021QE175), Major innovation projects for integrating science, education & industry of Qilu University of Technology (Shandong Academy of Sciences) (Grant No. 2022JBZ01–07), Jinan Talent Project (2020GXRC044), and the New Colleges and Universities Twenty Foundational Projects of Jinan City (2021GXRC068).

ORCID

Manman Ren https://orcid.org/0000-0002-7727-0370

References

1. T. Yang, J. Xia, Z. Piao, L. Yang, S. Zhang, Y. Xing, and G. Zhou, *ACS Nano*, **15**, 13901 (2021).
2. F. Qi, Z. Sun, X. Fan, Z. Wang, Y. Shi, G. Hu, and F. Li, *Adv. Energy Mater.*, **11**, 2100387 (2021).
3. J. Wang and W. Q. Han, *Adv. Funct. Mater.*, **32**, 2107166 (2021).
4. H. J. Peng, J. Q. Huang, and Q. Zhang, *Chem. Soc. Rev.*, **46**, 5237 (2017).
5. H. Hao, T. Hutter, B. L. Boyce, J. Watt, P. Liu, and D. Mitlin, *Chem. Rev.*, **122**, 8053 (2022).
6. R. Gao et al., *Adv. Funct. Mater.*, **32**, 2110313 (2021).
7. Y. Xie, J. Cao, X. Wang, W. Li, L. Deng, S. Ma, H. Zhang, C. Guan, and W. Huang, *Nano Lett.*, **21**, 8579 (2021).
8. H. Shi, G. Wen, Y. Nie, G. Zhang, and H. Duan, *Nanoscale*, **12**, 5261 (2020).
9. T. Feng, T. Zhao, S. Zhu, N. Zhang, Z. Wei, K. Wang, L. Li, F. Wu, and R. Chen, *Small Methods*, **5**, 2100649 (2021).
10. Y. Mao, W. Sun, X. Yue, W. Hou, T. Deng, L. He, L. Fang, R. Sun, Z. Wang, and K. Sun, *J. Power Sources*, **506**, 230254 (2021).
11. C. Xie, H. Shan, X. Song, L. Chen, J. Wang, J. W. Shi, J. Hu, J. Zhang, and X. Li, *J. Colloid Interface Sci.*, **592**, 448 (2021).
12. Y. Mao, G. Li, Y. Guo, Z. Li, C. Liang, X. Peng, and Z. Lin, *Nat. Commun.*, **8**, 14628 (2017).
13. Y. Zhang, Z. Gao, N. Song, J. He, and X. Li, *Materials Today Energy*, **9**, 319 (2018).
14. Z. Wang et al., *Adv. Mater.*, **31**, 1902228 (2019).
15. Y. Gao, Q. Guo, Q. Zhang, Y. Cui, and Z. Zheng, *Adv. Energy Mater.*, **11**, 2002580 (2020).
16. R. Elazari, G. Salitra, A. Garsuch, A. Panchenko, and D. Aurbach, *Adv. Mater.*, **23**, 5641 (2011).
17. Y. Zhang, G. Li, J. Wang, D. Luo, Z. Sun, Y. Zhao, A. Yu, X. Wang, and Z. Chen, *Adv. Energy Mater.*, **11**, 2100497 (2021).
18. D. Cai, L. Wang, L. Li, Y. Zhang, J. Li, D. Chen, H. Tu, and W. Han, *J. Mater. Chem. A*, **7**, 806 (2019).
19. D. Yang et al., *Adv. Energy Mater.*, **11**, 2101250 (2021).
20. T. Xiao, F. Yi, M. Yang, W. Liu, M. Li, M. Ren, X. Zhang, and Z. Zhou, *J. Mater. Chem. A*, **9**, 16692 (2021).
21. Y. C. Jiang, H. M. U. Arshad, H. J. Li, S. Liu, G. R. Li, and X. P. Gao, *Small*, **17**, 2005332 (2021).
22. K. Guo, G. Qu, J. Li, H. Xia, W. Yan, J. Fu, P. Yuan, and J. Zhang, *Energy Storage Mater.*, **36**, 496 (2021).
23. W. Xiao, Q. He, and Y. Zhao, *Appl. Surf. Sci.*, **570**, 151213 (2021).
24. Z. Ren, Z. Zhao, K. Zhang, X. Wang, and Y. Wang, *ChemElectroChem*, **8**, 1531 (2021).
25. L. Shi, W. Yuan, J. Liu, W. Zhang, S. Hou, and C. Hu, *J. Alloys Compd.*, **875**, 160045 (2021).
26. M. Zhao, X.-Y. Li, X. Chen, B.-Q. Li, S. Kaskel, Q. Zhang, and J.-Q. Huang, *eScience*, **1**, 44 (2021).
27. Z. Ye, Y. Jiang, T. Yang, L. Li, F. Wu, and R. Chen, *Adv Sci (Weinh)*, **9**, 2103456 (2022).
28. X. Yun, T. Lu, R. Zhou, Z. Lu, J. Li, and Y. Zhu, *Chem. Eng. J.*, **426**, 131328 (2021).
29. C. Zhang, J. J. Biendicho, T. Zhang, R. Du, J. Li, X. Yang, J. Arbiol, Y. Zhou, J. R. Morante, and A. Cabot, *Adv. Funct. Mater.*, **29**, 1903842 (2019).
30. T. Chen, Z. Shang, B. Yuan, N. Wu, M. Abuzar, J. Yang, X. Gu, C. Miao, M. Ling, and S. Li, *Energy Technology*, **8**, 2000302 (2020).
31. K. Xiao, J. Wang, Z. Chen, Y. Qian, Z. Liu, L. Zhang, X. Chen, J. Liu, X. Fan, and Z. X. Shen, *Small*, **15**, 1901454 (2019).
32. X. Liao et al., *ACS Appl. Mater. Interfaces*, **12**, 9181 (2020).
33. X. Huang, S. Men, H. Zheng, D. D. Qin, and X. Kang, *Chem. Asian J.*, **15**, 1456 (2020).
34. R. Wang, W. Tang, M. Tang, Q. Wu, and J. Li, *ACS Appl. Mater. Interfaces*, **13**, 21544 (2021).
35. H. Su, L. Lu, M. Yang, F. Cai, W. Liu, M. Li, X. Hu, M. Ren, X. Zhang, and Z. Zhou, *Chem. Eng. J.*, **429**, 132167 (2022).
36. H. Liu, H. Guo, N. Wu, W. Yao, R. Xue, M. Wang, and W. Yang, *J. Alloys Compd.*, **856**, 156535 (2021).
37. M. Yousaf et al., *Adv Sci (Weinh)*, **7**, 1902907 (2020).
38. Y. Sun, K. Xu, Z. Wei, H. Li, T. Zhang, X. Li, W. Cai, J. Ma, H. J. Fan, and Y. Li, *Adv. Mater.*, **30**, 1802121 (2018).
39. C. Zhou, P. Zhang, W. Wang, Y. Yang, W. Wang, H. Ding, X. Xu, W. Ji, and L. Chen, *Appl. Surf. Sci.*, **567**, 150784 (2021).
40. H. Yuan, H.-J. Peng, B.-Q. Li, J. Xie, L. Kong, M. Zhao, X. Chen, J.-Q. Huang, and Q. Zhang, *Adv. Energy Mater.*, **9**, 1802768 (2019).
41. H. Guo, G. Liu, M. Wang, Y. Zhang, W. Li, K. Chen, Y. Liu, M. Yue, and Y. Wang, *Chem. Asian J.*, **15**, 1493 (2020).
42. M. Li, S. Ji, X. Ma, H. Wang, X. Wang, V. Linkov, and R. Wang, *ACS Appl. Mater. Interfaces*, **14**, 16310 (2022).
43. B. Jiang et al., *Adv. Energy Mater.*, **11**, 2102995 (2021).
44. G. Li, W. Lei, D. Luo, Y. Deng, Z. Deng, D. Wang, A. Yu, and Z. Chen, *Energy Environ. Sci.*, **11**, 2372 (2018).
45. Y. Qiu, L. Fan, M. Wang, X. Yin, X. Wu, X. Sun, D. Tian, B. Guan, D. Tang, and N. Zhang, *ACS Nano*, **14**, 16105 (2020).
46. X. Tao et al., *Nat. Commun.*, **7**, 11203 (2016).
47. Z. Ye, Y. Jiang, L. Li, F. Wu, and R. Chen, *Adv. Mater.*, **32**, e2002168 (2020).
48. S. Chen, J. Zhang, Z. Wang, L. Nie, X. Hu, Y. Yu, and W. Liu, *Nano Lett.*, **21**, 5285 (2021).
49. C. Wen, X. Du, F. Wu, L. Wu, J. Li, and G. Liu, *ACS Appl. Mater. Interfaces*, **13**, 44389 (2021).
50. L. Chen, W. Yang, J. Liu, and Y. Zhou, *Nano Res.*, **12**, 2743 (2019).
51. L. Yang et al., *J. Power Sources*, **501**, 230040 (2021).
52. Y. Liu et al., *Adv. Funct. Mater.*, **32**, 2109462 (2021).
53. T. Xiao, L. Zhao, H. Ge, M. Yang, W. Liu, G. Li, M. Ren, X. Zhang, and Z. Zhou, *Chem. Eng. J.*, **439**, 135790 (2022).
54. G. Qu, K. Guo, J. Dong, H. Huang, P. Yuan, Y. Wang, H. Yuan, L. Zheng, and J.-N. Zhang, *Energy Storage Mater.*, **55**, 490 (2023).
55. Y. Yang et al., *ACS Appl. Mater. Interfaces*, **13**, 33066 (2021).
56. C. Guo, M. Liu, G. K. Gao, X. Tian, J. Zhou, L. Z. Dong, Q. Li, Y. Chen, S. L. Li, and Y. Q. Lan, *Angew. Chem. Int. Ed. Engl.*, **61**, e202113315 (2022).
57. Q. Li, Z. Ma, J. Zhao, K. Shen, T. Shi, Y. Xie, Y. Fan, X. Qin, and G. Shao, *J. Power Sources*, **521**, 230929 (2022).